Chemistry–A European Journal

Communication
doi.org/10.1002/chem.201905252

ChemPubSoc Europe
European Chemical Societies Publishing

Check for updates

Graphene | *Hot Paper* |

Room-Temperature Transport Properties of Graphene with Defects Derived from Oxo-Graphene

Zhenping Wang,[a] Qirong Yao,[b] and Siegfried Eigler*[a]

Abstract: In recent years, graphene oxide has been considered as a soluble precursor of graphene for electronic applications. However, the performance lags behind that of graphene due to lattice defects. Here, the relation between the density of defects in the range of 0.2% and 1.5% and the transport properties is quantitatively studied. Therefore, the related flakes of monolayers of graphene were prepared from oxo-functionalized graphene (oxo-G). The morphologic structure of oxo-G was imaged by atomic force microscopy (AFM) and scanning tunneling microscopy (STM). Field-effect mobility values were determined to range between 0.3 $cm^2V^{-1}s^{-1}$ and 33.2 $cm^2V^{-1}s^{-1}$, which were inversely proportional to the density of defects. These results provide the first quantitative description of the density of defects and transport properties, which plays an important role for potential applications.

Chemically modified graphene, such as graphene oxide (GO) or oxo-functionalized graphene (oxo-G), has received considerable interests for electronic,[1] optoelectronic,[2] biological[3] and chemical sensing[4] applications due to its physicochemical phenomena, including its tunable bandgap,[5] diverse luminescence behaviors,[6] biological compatibility[7] and the ability to modify the surface covalently and non-covalently.[8] In contrast to pristine graphene with carbon atoms arranged into a two-dimensional hexagonal lattice, oxo-G consists of abundant sp^3-hybridized carbon atoms, which are covalently bound to oxo-groups, mainly hydroxyl and epoxy groups.[9] The sp^3-portion is between 4% and 60%, with variable functionality.[10] The oxo-addends are tentatively immobilized onto segregated carbon, which isolates intact nanometer-scale graphene domains into small islands.[11] The existence of surface oxo-groups has profound impacts on improving its hydrophilicity,[12] chemical reactivity,[13] catalytic activity,[14] and optical properties,[2a] whereas the effect is detrimental for the electrical conductivity.[15] Therefore, to enhance the electrical performance of GO or oxo-G, extensive researches were conducted on the deoxygenation of oxo-addends.[16] In this regard, thermal processing provides a simple and versatile method for carbonization, however, without a carbon source, more lattice defects, such as few-atoms vacancies and nanometer-scale holes, are introduced due to thermal disproportionation along with CO_2 formation.[17] During the oxidative synthesis of GO and oxo-G, defects are introduced into the carbon framework.[10a] They cannot be healed out by simple chemical reduction although oxo-addends are reductively defunctionalized from the carbon lattice by a chemical reductant.[18] The defect concentration in GO or oxo-G can be determined by Raman spectroscopy after chemical reduction and typically varies from 0.001% to 2%.[19]

We demonstrated that the mobility of charge carriers of reduced oxo-G with a density of defects as low as 0.02% is exceeding 1000 $cm^2V^{-1}s^{-1}$, measured at 1.6 K in a Hall bar configuration and about 200 $cm^2V^{-1}s^{-1}$ for a density of defects of about 0.3%.[20] Those values are state-of-the art, but a series of questions arise. No systematic investigation is available relating the density of defects to the charge carrier mobilities at room temperature. Most reported values of carrier mobility values had been determined from multilayer thin films of reduced GO related materials with unknown thickness and qualities. Moreover, taking various synthetic procedures of oxo-G and non-standard transport measurements into consideration, there exist more uncertainties.

Here, we analyzed the structural evolution of single-layer oxo-G with defects from 0.2% to 1.5% by using AFM, STM and Raman spectroscopy. In addition, we investigated the effect of structural defects on the electrical properties of monolayer oxo-G by two-probe measurements under ambient conditions. Our results quantify the correspondence relationship between structural defects and transport capacities in high-defect single-layer graphene materials.

As shown in Figure 1, there are two types of graphene used in our investigation, almost defect-free graphene as reference sample prepared through tape exfoliation,[21] termed as $G_{0\%}$ (index indicates the density of defects, $I_D/I_G = 0.2 \pm 0.07$, which relates to a density of defects of 0.001%, abbreviated $G_{0\%}$) and

[a] Z. Wang, Prof. Dr. S. Eigler
Institute for Chemistry and Biochemistry, Freie Universität Berlin
Takustraße 3, 14195 Berlin (Germany)
E-mail: siegfried.eigler@fu-berlin.de

[b] Dr. Q. Yao
Physics of Interfaces and Nanomaterial, University of Twente
Enschede, 7500 AE (The Netherlands)

Supporting information and the ORCID identification number(s) for the author(s) of this article can be found under: https://doi.org/10.1002/chem.201905252.

© 2019 The Authors. Published by Wiley-VCH Verlag GmbH & Co. KGaA. This is an open access article under the terms of the Creative Commons Attribution License, which permits use, distribution and reproduction in any medium, provided the original work is properly cited.

Part of a Special Issue focusing on the "Chemical Functionalization of 2D Materials", which supports the symposium on the topic held at the E-MRS 2020 Spring Meeting. To view the complete issue, visit Issue 29.

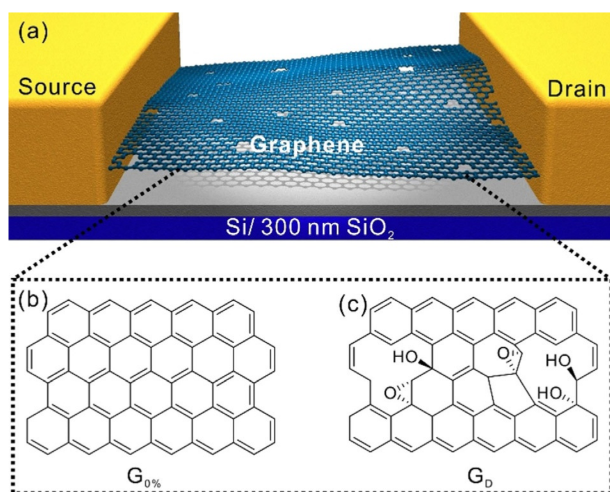

Figure 1. (a) Three-dimensional schematic of a graphene-based field-effect transistor (FET). Schematic illustration of the chemical structure of (b) defect-free graphene ($G_{0\%}$) and (c) graphene with defects (G_D).

graphene with various densities of defects (termed as G_D with density if defects between 0.2% and up to 1.5% determined by the relation to I_D/I_G ratios, compare Figure S1, Supporting Information) obtained by wet-chemical preparation and reduction with hydroiodic acid (HI).[20a] Surface morphologies of the samples were measured by atomic force microscopy (AFM) in tapping mode. As shown in Figure 2a, the average height of $G_{0\%}$ is determined to about 0.5 nm with lateral dimensions of 10–20 μm. Contaminants are visible at the edge of the $G_{0\%}$ sheet, which stems from the used tape during the exfoliation and transfer processes. In contrast, the roughness of G_D is with 1.0 nm twice as high as for $G_{0\%}$ due to bitopic oxo-groups at the carbon basal plane and possible adsorbates (Figure 2b). The lateral size of the depicted G_D flake was determined to be about 20 μm. To obtain information on the local atomic structure, scanning tunneling microscopy (STM) was used. Comparing the atomically-resolved honeycomb structure for defect-free highly ordered pyrolytic graphite (HOPG) in Figure 2c, the single-layer G_D reveals distinguishable topographical features with the appearance of islands and rows at bright spots, as depicted in Figure 2d. The amorphous networks arise from the presence of defects in the carbon lattices, such as residual oxo-groups, presumably at defect-sites, vacancies and nm-scale holes, as evidenced before.[10b,17a,22]

The density of defects in single layers of graphene can be quantified by Raman spectroscopy. Figure 3a shows the evolution of Raman spectra obtained from single layers of graphene with various densities of defects. For the monolayer $G_{0\%}$, there are two distinct peaks, the G band (at 1570 cm^{-1}), associated with the in-plane stretching vibration of C–C bonds, and the 2D band (at 2670 cm^{-1}), activated by a double-resonant Raman scattering.[23] The G and 2D bands are sensitive to the structure of the carbon hexagonal lattice and, thus, they can

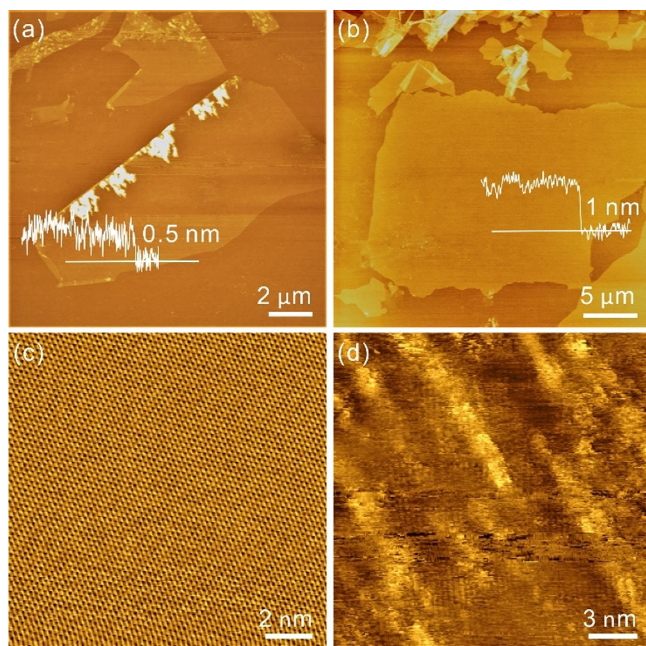

Figure 2. (a, b) AFM images of single-layer $G_{0\%}$ flake on a Si/SiO_2 substrate and a single-layer G_D flake on a Si/SiO_2 substrate. (c, d) High-resolution STM topographic images of HOPG and a single-layer G_D flake on HOPG.

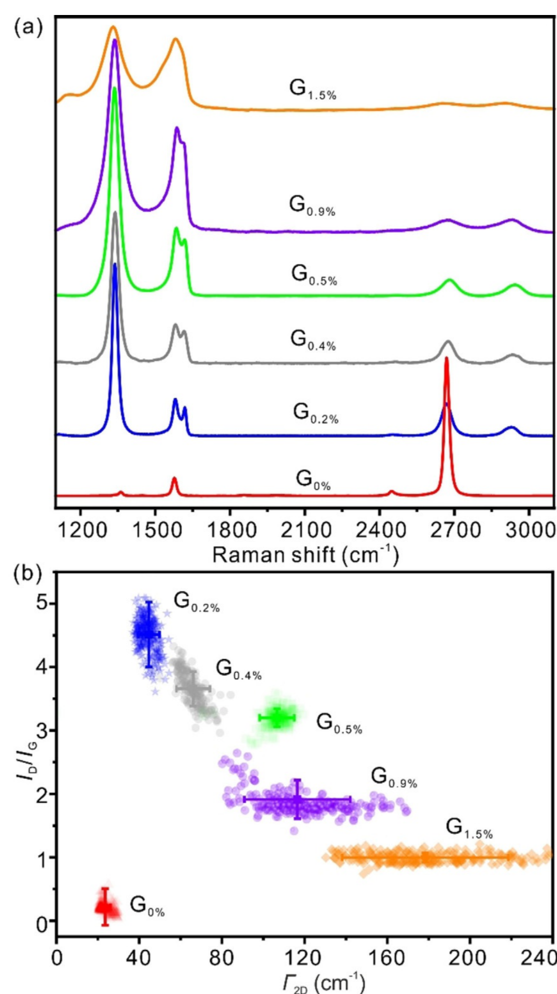

Figure 3. (a) Raman spectra obtained with a 532 nm excitation laser for single-layer graphene with various densities of defects, namely $G_{0\%}$, $G_{0.2\%}$, $G_{0.4\%}$, $G_{0.5\%}$, $G_{0.9\%}$ and $G_{1.5\%}$. (b) Corresponding plot of the I_D/I_G ratio vs. Γ_{2D}.

© 2019 The Authors. Published by Wiley-VCH Verlag GmbH & Co. KGaA, Weinheim

be used to characterize the quality of graphene-based materials. In addition, a faint D band at around 1360 cm^{-1} is noticed, probably evolving from grain boundaries or other lattice imperfections.[24] The structural defects can be estimated by using the defect-activated D band. Moreover, the intensity and shape of these peaks strongly depend on the nature of disorder. As the amount of disorder in graphene increases, the D-band intensities enhance, whereas the 2D-band intensities decrease. Further, the G-band splits into two sub-bands, G band (1583 cm^{-1}) and D′ band (1620 cm^{-1}). In addition, the broadening of all bands is observed with increasing density of defects. The full-width-at-half-maximum (FWHM, Γ) of the 2D peak (Γ_{2D}) increases from approximately 24 cm^{-1} in the single-layer $G_{0\%}$ to about 178 cm^{-1} in the single-layer $G_{1.5\%}$. In Table 1, the details of Raman peak analyses are summarized for graphene samples with different densities of defects, namely $G_{0\%}$, $G_{0.2\%}$, $G_{0.4\%}$, $G_{0.5\%}$, $G_{0.9\%}$ and $G_{1.5\%}$.

The intensity ratio of I_D/I_G is used for determining the density of defects in the G_D samples. In the case of single-layer $G_{0\%}$, it contains an extremely low density of defects, which belongs to the low-defect density regime according to the Raman model introduced by Lucchese, Cançado and Ferrari et al., with a ratio of $I_D/I_G = 0.2 \pm 0.07$ corresponding to about 24000 C atoms within the intact graphene lattice. According to Equation (1):

$$N_C = 2L_D^2 2D_D^2/A_{cell} \quad (1)$$

in which the N_C corresponds to intact carbon atoms and $A_{cell} = 0.246^2 \times \sin(60^\circ) = 0.05239$ nm^2, the average distance between defects L_D is about 25 nm. The related defect density (n_D) is about 5.1×10^{10} cm^{-2}, using $n_D(cm^{-2}) = 10^{14}/(\pi L_D^2)$.[19b] However, the investigated G_D samples relate to the high-defect density regime. In this regime, the I_D/I_G ratio increases with an increase of L_D, based on the relation of $I_D/I_G \propto L_D \propto N_C$.[19b] Accordingly, the density of defects increases from 0.3% to 1.5%, the corresponding I_D/I_G ratio decreases from 4.5 to 1.0 and the L_D values gradually decrease from 3.5 nm to 1.3 nm, respectively. The related n_D increases from about 2.6×10^{12} cm^{-2} to 1.9×10^{13} cm^{-2}. As depicted in Figure 3b, the evolution of qualities in the yielded graphene samples are illustrated by plotting the I_D/I_G ratio versus Γ_{2D}. With increasing the density of defects, the Γ_{2D} values increase, which is consistent with our discussion above.

Field-effect transistors were fabricated by using the obtained monolayer graphene samples as conducting channels (Figure 4a). The monolayer $G_{0\%}$ flakes were mechanically exfoliated from a bulk graphite and transferred to a heavily p-doped Si substrate with a 300 nm thick SiO_2 layer (Si/SiO_2),[21] which acts as the reference sample. The Γ_{2D} value of 23.6 ± 2.6 and $I_{2D}/I_G >$ 4 was determined by Raman spectroscopy to prove the single-layer nature of the produced flake (Figure 3a). The monolayer G_D flakes prepared by wet-chemistry were deposited on Si/SiO_2 substrates by using Langmuir–Blodgett technique and subsequent chemical reduction or thermal processing.[20a] An AFM image of $G_{0.5\%}$ FET device is shown in Figure 4b and a height profile of monolayer $G_{0.5\%}$ flake with about 1.2 nm is depicted in Figure 4c.The Si/SiO_2 substrate serves as a back-gate. The metal contacts Cr/Au (5 nm/70 nm), served as source and drain electrodes, were deposited onto single-layer graphene channel materials by using e-beam lithography and evaporation pro-

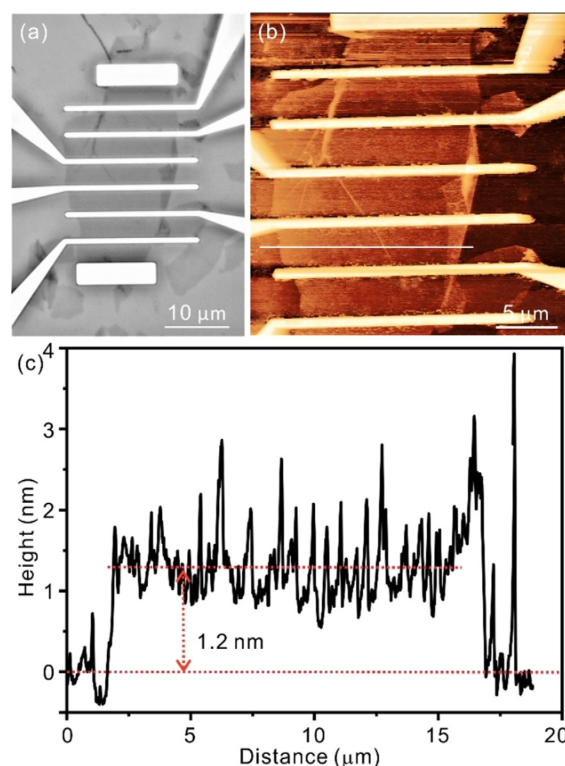

Figure 4. (a) Optical microscope image of $G_{0.5\%}$ field-effect transistor (FET). The monolayer $G_{0.5\%}$ flake is the channel material. The Si/300 nm SiO_2 substrate acts as a back-gate. The Cr/Au (5 nm/70 nm) contacts are used for two-probe connection. (b) AFM image of $G_{0.5\%}$ FET device. (c) Height profile of the monolayer $G_{0.5\%}$ flake along grey line shown in (b).

Table 1. Summary of the results of fitting Raman spectra by Lorentz functions for the yielded monolayer graphene with defects densities of 0%, 0.2%, 0.4%, 0.5%, 0.9% and 1.5%.

Sample	Γ_D [cm^{-1}]	Γ_G [cm^{-1}]	Γ_{2D} [cm^{-1}]	I_D/I_G	N_C	L_D [nm]	n_D [cm^{-2}]
$G_{0\%}$	≈ 0	14.2 ± 4.8	23.6 ± 2.6	0.2 ± 0.07	$> 24 \times 10^3$	> 25	$\approx 5.1 \times 10^{10}$
$G_{0.2\%}$	25.2 ± 3.0	40.5 ± 8.5	44.7 ± 5.1	4.5 ± 0.5	454 ± 49	3.5 ± 0.19	$\approx 2.6 \times 10^{12}$
$G_{0.4\%}$	38.1 ± 2.9	41.3 ± 3.1	66.1 ± 8.1	3.7 ± 0.2	232 ± 25	2.5 ± 0.13	$\approx 5.1 \times 10^{12}$
$G_{0.5\%}$	46.3 ± 3.9	33.7 ± 3.0	106.9 ± 5.6	3.2 ± 0.1	180 ± 9	2.2 ± 0.05	$\approx 6.6 \times 10^{12}$
$G_{0.9\%}$	67.5 ± 6.4	58.5 ± 27.1	118.6 ± 18.6	1.9 ± 0.2	107 ± 7	1.7 ± 0.06	$\approx 1.1 \times 10^{13}$
$G_{1.5\%}$	91.0 ± 5.7	120.3 ± 42.4	178.3 ± 40.1	1.0 ± 0.1	63 ± 3	1.3 ± 0.03	$\approx 1.9 \times 10^{13}$

© 2019 The Authors. Published by Wiley-VCH Verlag GmbH & Co. KGaA, Weinheim

cesses. Avoiding any thermal decomposition of chemically-derived G_D samples, no annealing process was performed for all prepared devices after the lift-off process.

Electrical transport measurements were performed at ambient conditions in a two-terminal configuration. The performance of transistors relies on the properties of channel materials, gate dielectrics, electrodes and test conditions. Therefore, to reliably compare electrical performances for the obtained monolayer graphene samples, all transistors were prepared with parallel electrodes, the same manufacturing processes and test conditions.

The Figure 5 presents the transfer characteristics of fabricated FET devices based on graphene samples with the defects from 0% to 1.5%. Linear output relations (I_{DS}–V_{DS}) are determined and visualized in the insets of Figure 5, indicating ohmic contacts between the graphene samples and the metal electrodes under ambient conditions. The $G_{0\%}$ device in Figure 5a shows V-shape transfer curves (I_{DS}–V_{BG}) with asymmetric Dirac voltage (corresponding to the minimum value of I_{DS}) located at +20 V. The observed p-doping behavior was probably attributed to the heavily p-doped Si/SiO_2 substrate, impurity doping as a result of exfoliation and transfer processes or polar adsorbates like water or oxygen acting as charge traps between substrate and the graphene surface. Furthermore, a hysteretic behavior between forward and reverse sweeps are observed. For G_D transistors (Figure 5b–f), no Dirac point appears within the range of the scanned gate voltages from −50 V to +50 V. All samples show unipolar p-type character. These defective G_D samples are stronger p-doped than the $G_{0\%}$ sample due to the oxo-groups modification of the graphene networks.[25]

The field-effect carrier mobilities were extracted by using Equation (2):[26]

$$\mu = (L/W) \times (1/C_{ox}V_{DS}) \times (dI_{DS}/dV_{BG}) \quad (2)$$

in which L and W are the channel length and width, respectively, and $C_{ox} = 1.15 \times 10^{-8}$ F cm^{-2} is the capacitance per unit area of the gate dielectric material. The room-temperature average mobility values of monolayers of G_D are determined between 33.2 cm^{2}V^{-1}s^{-1} and 0.3 cm^{2}V^{-1}s^{-1} for densities of defects between 0.2% and 1.5%. The mobility values are significantly lower than the value of 685 cm^{2}V^{-1}s^{-1} obtained for our defect-free $G_{0\%}$ and not annealed reference sample. In addition, in Figure 6 the field-effect mobilities are plotted as a function of number of C atom (N_C) and distance between defects (L_D), respectively. It is found that the mobilities follow, within

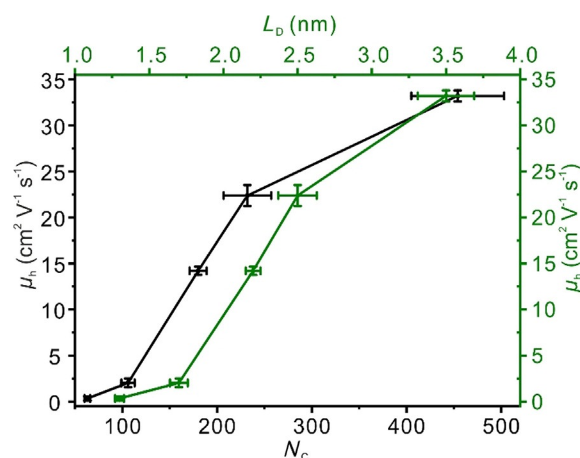

Figure 6. Field-effect carrier mobility values as a function of number of C atoms (N_C) of intact graphene areas (black curve) and the distance of defects L_D (green curve). The error bars shown are based on the data of Table 1 and Figure S2 (Supporting Information).

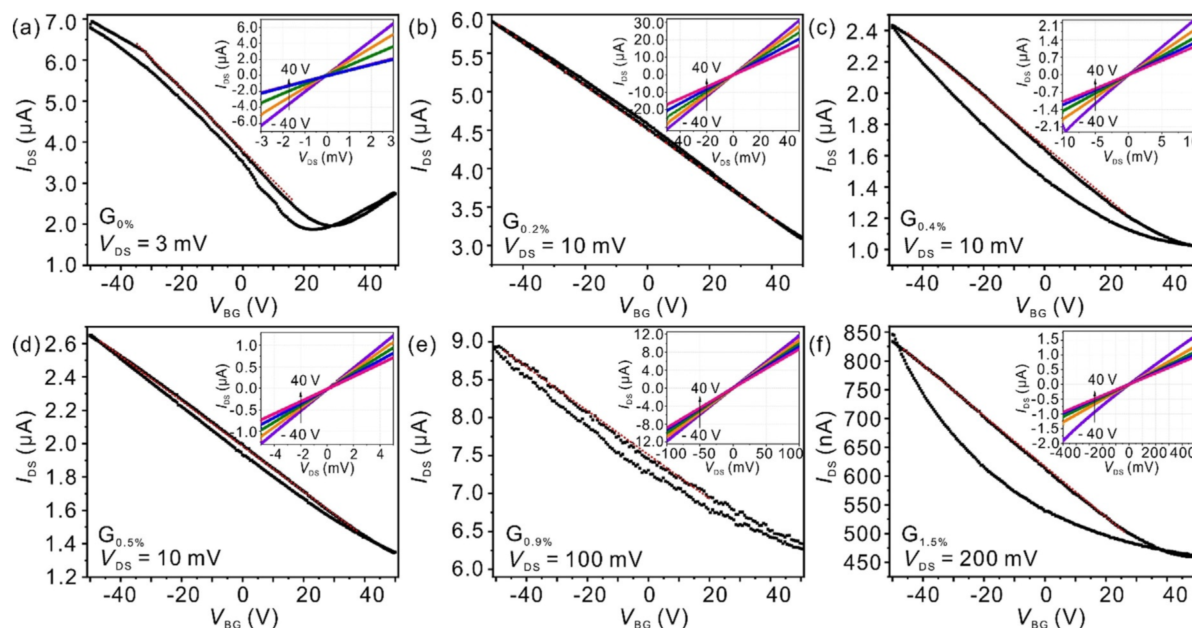

Figure 5. Room-temperature transfer characteristics of graphene transistors with densities of defects of 0%, 0.2%, 0.4%, 0.5%, 0.9% and 1.5% (a–f), respectively. The gate voltage is swept continuously from −50 V to 50 V and back to −50 V. The inset shows the corresponding output curves.

© 2019 The Authors. Published by Wiley-VCH Verlag GmbH & Co. KGaA, Weinheim

experimental uncertainties, a nonlinear relationship with L_D and N_C, because the defect-free area of graphene increases over-proportionally with increasing L_D.

In summary, we have studied the room-temperature electrical properties of single-layer graphene derived from oxo-G containing defect densities varying from 0.2% to 1.5%. The defects give rise to a heterogeneous topographical morphology of oxo-G. The isolated graphene domains ($L_D \leq 3$ nm) in oxo-G were identified by Raman spectroscopy. The isolation of these domains limits the charge transport in reduced oxo-G. Therefore, the mobility values of charge carriers of graphene with densities of defects between 0.2% and 1.5%, change by three orders of magnitude, from 0.3 $cm^2V^{-1}s^{-1}$ and 33.2 cm^2V^{-1s-1}. More generally, the mobility of charge carriers varies by orders of magnitude, although it looks like that the density of defects varies only a little. The fundamental findings reported here can explain the generally diverging results often reported for reduced graphene oxide used in applications.

Experimental Section

Methods

AFM characterization was performed by using a JPK NanoWizard 4 Atomic Force Microscope in tapping mode at room temperature. Raman characterization was carried out with a Horiba Explorer spectrometer with a 532 nm laser for excitation under air conditions. Scanning tunneling microscopy (STM) was conducted by using Omicron-STM1 microscope under ultra-high vacuum ($<10^{-10}$ mbar). All transport measurements were performed under ambient conditions by a two-probe station and two source-measurement units (Keithley 2450).

Preparation of defect-free $G_{0\%}$ flakes

The defect-free monolayer $G_{0\%}$ flakes were prepared by micromechanical exfoliation and then transferred on Si/SiO_2 substrates as reported methods.[21]

Preparation of defective G_D from oxo-G

The defective G_D flakes were prepared by low-temperature oxidation of graphite based by the before reported method of our group.[20a] Then, the oxo-G was dissolved in methanol/water 1:1 mixtures. The monolayer flakes of G_D were deposited onto the Si/SiO_2 substrate by using the Langmuir–Blodgett technique (LB, Kibron MicroTrough, 3 $mN\,m^{-1}$ with the surface tension of water as reference value of 72.8 $mN\,m^{-1}$). Reduction was performed by vapor of hydriodic acid (HI) and trifluoroacetic acid (TFA) (1:1, *v/v*) at 80 °C (10 min). Subsequently, the surface of G_D was cleaned with doubly distilled water (Carl Roth) to remove iodine species. The density of defects of individual flakes was determined by Raman spectroscopy (Horiba Explorer spectrometer with a 532 nm laser for excitation under air conditions). Subsequently, flakes with defined density of defects were selected for FET device fabrication.

Fabrication of FET devices

Standard electron beam lithography procedure (Raith PIONEER TWO) was used to define and expose the geometry of metal contacts. Subsequently, a 5 nm/70 nm Cr/Au layer was deposited with thermal evaporation (Kurt J. Lesker NANO 36) and lifted off in acetone to make electrode contact to monolayer $G_{0\%}$ and G_D flakes, respectively.

Acknowledgements

This research is supported by the China Scholarship Council (CSC), the Deutsche Forschungsgemeinschaft (DFG, German Research Foundation), project number 392444269.

Conflict of interest

The authors declare no conflict of interest.

Keywords: defects · electronic transport · graphene · graphene oxide

[1] a) G. Eda, G. Fanchini, M. Chhowalla, *Nat. Nanotechnol.* **2008**, *3*, 270–274; b) D. S. Hecht, L. B. Hu, G. Irvin, *Adv. Mater.* **2011**, *23*, 1482–1513; c) X. Huang, Z. Y. Zeng, Z. X. Fan, J. Q. Liu, H. Zhang, *Adv. Mater.* **2012**, *24*, 5979–6004.
[2] a) K. P. Loh, Q. L. Bao, G. Eda, M. Chhowalla, *Nat. Chem.* **2010**, *2*, 1015–1024; b) Q. L. Bao, K. P. Loh, *ACS Nano* **2012**, *6*, 3677–3694; c) J. H. Du, S. F. Pei, L. P. Ma, H. M. Cheng, *Adv. Mater.* **2014**, *26*, 1958–1991.
[3] a) C. Chung, Y. K. Kim, D. Shin, S. R. Ryoo, B. H. Hong, D. H. Min, *Acc. Chem. Res.* **2013**, *46*, 2211–2224; b) V. C. Sanchez, A. Jachak, R. H. Hurt, A. B. Kane, *Chem. Res. Toxicol.* **2012**, *25*, 15–34.
[4] a) W. J. Yuan, G. Q. Shi, *J. Mater. Chem. A* **2013**, *1*, 10078–10091; b) S. X. Wu, Q. Y. He, C. L. Tan, Y. D. Wang, H. Zhang, *Small* **2013**, *9*, 1160–1172.
[5] a) L. Guo, R. Q. Shao, Y. L. Zhang, H. B. Jiang, X. B. Li, S. Y. Xie, B. B. Xu, Q. D. Chen, J. F. Song, H. B. Sun, *J. Phys. Chem. C* **2012**, *116*, 3594–3599; b) T. Tsuchiya, K. Terabe, M. Aono, *Adv. Mater.* **2014**, *26*, 1087–1091.
[6] a) Q. S. Mei, B. H. Liu, G. M. Han, R. Y. Liu, M. Y. Han, Z. P. Zhang, *Adv. Sci.* **2019**, *6*, 1900855; b) S. Vempati, T. Uyar, *Phys. Chem. Chem. Phys.* **2014**, *16*, 21183–21203.
[7] H. C. Zhang, G. Gruner, Y. L. Zhao, *J. Mater. Chem. B* **2013**, *1*, 2542–2567.
[8] a) H. Y. Mao, Y. H. Lu, J. D. Lin, S. Zhong, A. T. S. Wee, W. Chen, *Prog. Surf. Sci.* **2013**, *88*, 132–159; b) V. Georgakilas, M. Otyepka, A. B. Bourlinos, V. Chandra, N. Kim, K. C. Kemp, P. Hobza, R. Zboril, K. S. Kim, *Chem. Rev.* **2012**, *112*, 6156–6214.
[9] a) D. R. Dreyer, A. D. Todd, C. W. Bielawski, *Chem. Soc. Rev.* **2014**, *43*, 5288–5301; b) A. Lerf, H. Y. He, T. Riedl, M. Forster, J. Klinowski, *Solid State Ionics* **1997**, *101*, 857–862; c) L. B. Casabianca, M. A. Shaibat, W. W. W. Cai, S. Park, R. Piner, R. S. Ruoff, Y. Ishii, *J. Am. Chem. Soc.* **2010**, *132*, 5672–5676.
[10] a) S. Eigler, *Chem. Eur. J.* **2016**, *22*, 7012–7027; b) P. Feicht, J. Biskupek, T. E. Gorelik, J. Renner, C. E. Halbig, M. Maranska, F. Puchtler, U. Kaiser, S. Eigler, *Chem. Eur. J.* **2019**, *25*, 8955–8959.
[11] C. Mattevi, G. Eda, S. Agnoli, S. Miller, K. A. Mkhoyan, O. Celik, D. Mastrogiovanni, G. Granozzi, E. Garfunkel, M. Chhowalla, *Adv. Funct. Mater.* **2009**, *19*, 2577–2583.
[12] S. Some, Y. Xu, Y. Kim, Y. Yoon, H. Qin, A. Kulkarni, T. Kim, H. Lee, *Sci. Rep.* **2013**, *3*, 1868.
[13] D. Matochová, M. Medved, A. Bakandritsos, T. Steklý, R. Zboril, M. Otyepka, *J. Phys. Chem. Lett.* **2018**, *9*, 3580–3585.
[14] X. K. Kong, C. L. Chen, Q. W. Chen, *Chem. Soc. Rev.* **2014**, *43*, 2841–2857.
[15] Q. B. Zheng, Z. G. Li, J. H. Yang, J. K. Kim, *Prog. Mater. Sci.* **2014**, *64*, 200–247.
[16] S. F. Pei, H. M. Cheng, *Carbon* **2012**, *50*, 3210–3228.
[17] a) F. Grote, C. Gruber, F. Börrnert, U. Kaiser, S. Eigler, *Angew. Chem. Int. Ed.* **2017**, *56*, 9222–9225; *Angew. Chem.* **2017**, *129*, 9350–9353; b) S. Grimm, M. Schweiger, S. Eigler, J. Zaumseil, *J. Phys. Chem. C* **2016**, *120*, 3036–3041.
[18] a) O. C. Compton, S. T. Nguyen, *Small* **2010**, *6*, 711–723; b) S. Eigler, S. Grimm, M. Enzelberger-Heim, P. Müller, A. Hirsch, *Chem. Commun.* **2013**,

 © 2019 The Authors. Published by Wiley-VCH Verlag GmbH & Co. KGaA, Weinheim

49, 7391 – 7393; c) K. W. Silverstein, C. E. Halbig, J. S. Mehta, A. Sharma, S. Eigler, J. M. Mativetsky, *Nanoscale* **2019**, *11*, 3112 – 3116; d) B. Butz, C. Dolle, C. E. Halbig, E. Spiecker, S. Eigler, *Angew. Chem. Int. Ed.* **2016**, *55*, 15771 – 15774; *Angew. Chem.* **2016**, *128*, 16003 – 16006; e) A. Kahnt, R. Flyunt, S. Naumov, W. Knolle, S. Eigler, R. Hermann, B. Abel, *RSC Adv.* **2016**, *6*, 68835 – 68845; f) R. Flyunt, W. Knolle, A. Kahnt, C. E. Halbig, A. Lotnyk, T. Häupl, A. Prager, S. Eigler, B. Abel, *Nanoscale* **2016**, *8*, 7572 – 7579.

[19] a) A. Jorio, L. G. Cançado, *Phys. Chem. Chem. Phys.* **2012**, *14*, 15246 – 15256; b) L. G. Cançado, A. Jorio, E. H. M. Ferreira, F. Stavale, C. A. Achete, R. B. Capaz, M. V. O. Moutinho, A. Lombardo, T. S. Kulmala, A. C. Ferrari, *Nano Lett.* **2011**, *11*, 3190 – 3196; c) S. Eigler, F. Hof, M. Enzelberger-Heim, S. Grimm, P. Müller, A. Hirsch, *J. Phys. Chem. C* **2014**, *118*, 7698 – 7704.

[20] a) S. Eigler, M. Enzelberger-Heim, S. Grimm, P. Hofmann, W. Kroener, A. Geworski, C. Dotzer, M. Rockert, J. Xiao, C. Papp, O. Lytken, H. P. Steinrück, P. Müller, A. Hirsch, *Adv. Mater.* **2013**, *25*, 3583 – 3587; b) Z. Wang, S. Eigler, M. Halik, *Appl. Phys. Lett.* **2014**, *104*, 243502.

[21] M. Yi, Z. G. Shen, *J. Mater. Chem. A* **2015**, *3*, 11700 – 11715.

[22] a) C. Gómez-Navarro, R. T. Weitz, A. M. Bittner, M. Scolari, A. Mews, M. Burghard, K. Kern, *Nano Lett.* **2009**, *9*, 2206 – 2206; b) S. Seiler, C. E. Halbig, F. Grote, P. Rietsch, F. Börrnert, U. Kaiser, B. Meyer, S. Eigler, *Nat. Commun.* **2018**, *9*, 836.

[23] A. C. Ferrari, D. M. Basko, *Nat. Nanotechnol.* **2013**, *8*, 235 – 246.

[24] L. G. Cançado, M. G. da Silva, E. H. M. Ferreira, F. Hof, K. Kampioti, K. Huang, A. Penicaud, C. A. Achete, R. B. Capaz, A. Jorio, *2D Mater.* **2017**, *4*, 025039.

[25] Z. Wang, Q. Yao, Y. Hu, C. Li, M. Hußmann, B. Weintrub, J. N. Kirchhof, K. Bolotin, T. Taniguchhi, K. Wantanabe, S. Eigler, *RSC Adv.* **2019**, *9*, 38011 – 38016.

[26] F. Schwierz, *Nat. Nanotechnol.* **2010**, *5*, 487 – 496.

Manuscript received: November 20, 2019
Revised manuscript received: December 17, 2019
Accepted manuscript online: December 18, 2019
Version of record online: February 3, 2020

 © 2019 The Authors. Published by Wiley-VCH Verlag GmbH & Co. KGaA, Weinheim